Research Square

Preprints are preliminary reports that have not undergone peer review.
They should not be considered conclusive, used to inform clinical practice,
or referenced by the media as validated information.

CuO/Cu-MOF-Loaded Hollow Mesoporous Zirconia Nanospheres as Microwave Transducers for Enhanced Thermal Ablation of Hepatocellular Carcinoma

Xiuxiu Hao
Second Affiliated Hospital of Chongqing Medical University
Wei Zhang
Second Affiliated Hospital of Chongqing Medical University
Liting He
Second Affiliated Hospital of Chongqing Medical University
Jie Zhou
Second Affiliated Hospital of Chongqing Medical University
Yun Zhou
Second Affiliated Hospital of Chongqing Medical University
Runmin Zha
Second Affiliated Hospital of Chongqing Medical University
Mao Tang
Second Affiliated Hospital of Chongqing Medical University
Min Zheng
Second Affiliated Hospital of Chongqing Medical University
Mingyuan Dai
Second Affiliated Hospital of Chongqing Medical University
Ping Liang
Chinese PLA General Hospital
Haitao Ran
ranhaitao@cqmu.edu.cn

Second Affiliated Hospital of Chongqing Medical University

Research Article

Keywords: Hepatocellular carcinoma, Microwave ablation, Hollow mesoporous zirconia, Copper-based metal-organic framework, Reactive oxygen species, Heat-sink effect

Posted Date: September 24th, 2026

DOI: https://doi.org/10.21203/rs.3.rs-10488087/v1

License: This work is licensed under a Creative Commons Attribution 4.0 International License.
Read Full License

Additional Declarations: No competing interests reported.

Abstract

Background

Microwave ablation (MWA) is widely used as a minimally invasive treatment for hepatocellular carcinoma (HCC); however, its therapeutic efficacy remains limited by insufficient ablation margins caused by the heat-sink effect near large vessels and collateral thermal injury associated with high-power irradiation. This study aimed to develop a microwave-responsive nanoplatform to enhance tumor ablation efficiency while reducing thermal damage to surrounding tissues.

Methods

Hollow mesoporous zirconia nanospheres loaded with CuO/Cu-metal–organic frameworks (Zr@C/C NPs) were fabricated using a hard-template strategy combined with vacuum-assisted infiltration. The physicochemical properties, microwave responsiveness, and biocompatibility of Zr@C/C NPs were characterized. Their therapeutic effects were evaluated in Hepa1-6 hepatocellular carcinoma cells and a rabbit VX2 liver tumor model with perivascular tumor implantation. The underlying antitumor mechanism was investigated by assessing reactive oxygen species (ROS) generation, apoptosis, and proliferation-associated biomarkers.

Results

Zr@C/C NPs exhibited a uniform hollow core–shell structure, high surface area (352–357 $m^2 g^{-1}$), and favorable colloidal stability. Under microwave irradiation (0.9 W, 5 min), Zr@C/C NPs markedly enhanced intracellular ROS generation by 7.8-fold compared with controls and induced apoptosis in 62.4% of Hepa1-6 cells under sublethal thermal conditions, while showing low intrinsic cytotoxicity toward HUVEC cells (> 77.5% viability at 100 μg mL^{-1}). In the perivascular VX2 liver tumor model, Zr@C/C NP-enhanced MWA at 30 W achieved a significantly larger coagulative necrosis volume than conventional MWA at 50 W (4.18 ± 0.35 cm^3 vs. 2.06 ± 0.22 cm^3, $p < 0.01$). Contrast-enhanced ultrasound demonstrated complete tumor non-perfusion after treatment, and no early recurrence was observed during the 30-day follow-up. Histological analysis revealed increased apoptosis at sublethal ablation margins and reduced Ki67 expression following Zr@C/C NP-mediated MWA.

Conclusions

Zr@C/C NPs act as effective microwave sensitizers by converting sublethal thermal energy into ROS-mediated cytotoxicity, thereby enhancing tumor ablation efficacy at reduced microwave power. This strategy provides a potential approach for overcoming heat-sink-related limitations and improving the safety and effectiveness of MWA for hepatocellular carcinoma.

Background

Hepatocellular carcinoma (HCC) is the most common primary liver malignancy and the third leading cause of cancer-related mortality worldwide. Microwave ablation (MWA) has become a cornerstone of locoregional therapy for early- and intermediate-stage HCC, offering advantages of rapid heating, large ablation volumes, and reduced susceptibility to the heat-sink effect compared to radiofrequency ablation. However, two clinical bottlenecks persist. First, tumors located near major hepatic vessels (> 3 mm diameter) remain incompletely ablated because convective blood flow dissipates thermal energy, preventing lethal temperatures from reaching the tumor margin. Second, the high microwave power (typically 50–70 W) required to overcome this heat-sink effect increases the risk of collateral thermal injury to adjacent bile ducts, gallbladder, bowel, and diaphragm. The resulting trade-off between oncological efficacy and periprocedural safety represents a fundamental limitation of current MWA technology.

To address these constraints, nanomaterial-based MWA sensitizers have emerged as a promising strategy. Mesoporous metal oxide nanoparticles, particularly zirconium dioxide (ZrO_2), have attracted attention due to their high specific surface area, tunable porosity, and excellent thermal stability. Copper (Cu), as a versatile transition metal, can amplify microwave-induced hyperthermia through dielectric loss and catalyze the generation of reactive oxygen species (ROS) via Fenton-like reactions [7]. However, monocomponent ZrO_2 exhibits suboptimal microwave-to-thermal conversion efficiency, while Cu-based nanoparticles are often limited by poor colloidal stability and dose-dependent cytotoxicity.

Several nanomaterial platforms have been explored as MWA sensitizers. Wang et al. demonstrated that mesoporous Fe_3O_4 nanoparticles elevated local temperatures during MWA [1], although thermal persistence remained suboptimal with rapid temperature decay post-irradiation. Li et al. reported Cu-doped TiO_2 nanoparticles that enhanced MWA-induced apoptosis, but the irregular mesoporous architecture restricted cargo loading capacity [2]. Zhang et al. identified that mesoporous ZrO_2 scaffolds improved microwave-to-thermal conversion, yet the platform lacked transition-metal-mediated bio-effects necessary for synergistic cytotoxicity [3]. Despite these advances, the rational integration of copper-based catalytic centers within a stable mesoporous ZrO_2 framework—designed specifically to convert sublethal microwave energy into chemical cytotoxicity—remains largely unexplored[4].

Here, we report the rational design of CuO/Cu-MOF-loaded hollow mesoporous ZrO_2 nanospheres (designated Zr@C/C NPs) as a microwave-responsive sensitizer for HCC ablation. The platform is built around three design principles: (i) a hollow ZrO_2 shell provides a thermally stable scaffold that enhances microwave absorption through multiple internal reflections; (ii) CuO/Cu-MOF catalytic centers loaded within the interior cavity generate ROS upon microwave excitation, converting sublethal thermal energy into chemical cytotoxicity within the heat-sink zone; and (iii) the mesoporous architecture enables efficient cargo loading while maintaining colloidal stability and biocompatibility. We characterize the structure, colloidal properties, and crystalline composition of Zr@C/C NPs, evaluate their ROS-generating capacity and tumor-cell-killing efficacy in vitro under simulated heat-sink conditions, and validate their

therapeutic performance and safety profile in a rabbit VX2 liver tumor model with perivascular tumor implantation. Our results demonstrate that this "thermal-kinetic" strategy achieves effective tumor ablation at reduced microwave power while maintaining vascular integrity, providing a preclinical basis for overcoming the efficacy-safety dilemma in MWA of HCC (See the Fig. 1) .

Methods

Materials and Chemicals

Zirconium (IV) propoxide (70 wt% in 1-propanol), copper (II) nitrate trihydrate ($Cu(NO_3)_2·3H_2O$, ≥ 99%), 1,4-benzenedicarboxylic acid (H_2BDC, 98%), polyvinylpyrrolidone (PVP, MW ~ 40,000), N,N-dimethylformamide (DMF, ≥ 99.8%), ammonia solution (25% NH_3 in H_2O), tetraethyl orthosilicate (TEOS, ≥ 99%), sodium hydroxide (NaOH, ≥ 98%), absolute ethanol, and acetonitrile were purchased from Sigma-Aldrich and used as received. Deionized water (dH_2O, 18.2 MΩ·cm) was produced using a Milli-Q system (Fig .1A).

Synthesis of Hollow Mesoporous ZrO_2 Nanospheres

Hollow mesoporous ZrO_2 nanospheres were fabricated via a hard-template method followed by selective etching [29, 40]. Silica nanospheres (SiO_2, average diameter 130 ~ 145 nm) were synthesized by the Stöber method. Briefly, 200 mg of SiO_2 nanospheres, 1.5 mL of ammonia (25%), and 0.6 mL of zirconium (IV) propoxide were homogeneously dispersed in a co-solvent system consisting of absolute ethanol and acetonitrile (volumetric ratio 3:1). Under continuous stirring for 6 h at room temperature, controlled hydrolysis and condensation of zirconium (IV) propoxide facilitated the in situ formation of a mesoporous ZrO_2 shell on the SiO_2 templates. The resulting ZrO_2@SiO_2 core-shell nanostructures were collected by centrifugation (8,000 rpm, 10 min) and washed three times with ethanol. To generate the hollow interior, the ZrO_2@SiO_2 nanospheres were redispersed in 150 mL of dH_2O and subjected to selective etching with 10 mL of 1 M NaOH at 80°C for 4 h. The purified hollow ZrO_2 nanospheres were collected by centrifugation, washed three times with dH_2O, and lyophilized for further use (Fig. 1A).

Synthesis of Zr@C/C NPs

Zr@C/C NPs were synthesized via a two-step process combining vacuum-assisted infiltration and solvothermal growth [6, 41]. First, 50 mg of hollow ZrO_2 nanospheres and 520 mg of $Cu(NO_3)_2·3H_2O$ were dissolved in 2 mL of dH_2O to form a homogeneous precursor solution. The $Cu(NO_3)_2$ precursor was loaded into the mesoporous cavities of the ZrO_2 nanospheres under vacuum negative pressure (− 0.1 MPa, 30 min), yielding the intermediate ZrO_2@$Cu(NO_3)_2$ composite. To facilitate in situ growth of the copper-based catalytic centers, 60 mg of PVP, the ZrO_2@$Cu(NO_3)_2$ composite, and 170 mg of H_2BDC were uniformly dispersed in 80 mL of DMF. The suspension was transferred into a 100 mL Teflon-lined stainless-steel autoclave and subjected to solvothermal reaction at 120°C for 10 h. During this process, thermal decomposition of $Cu(NO_3)_2$ produced CuO species, while simultaneous coordination between Cu^{2+} and the carboxylate groups of H_2BDC led to crystallization of a Cu-based metal-organic framework

(Cu-MOF) within the ZrO_2 cavity. The resulting product was collected by centrifugation, washed three times with DMF and ethanol, and dried under vacuum at 60°C (Fig .1A).

Physicochemical Characterization

Morphology and structural evolution were visualized by transmission electron microscopy (TEM, JEM-2100, JEOL) operated at 200 kV [45]. Elemental mapping was performed by energy-dispersive X-ray spectroscopy (EDS) coupled with TEM to verify the spatial distribution of Zr, O, and Cu [17]. Crystalline phases were identified by X-ray diffraction (XRD, Bruker D8 Advance) using Cu Kα radiation (λ = 1.5406 Å), with a scanning range of 10° to 80° and a step size of 0.02° [44]. Fourier transform infrared (FTIR) spectra were recorded on a Nicolet iS50 spectrometer (Thermo Fisher) using KBr pellets in the range of 400–4000 cm^{-1} [6, 43]. Zeta potential and hydrodynamic size were measured using a Malvern Zetasizer Nano ZS at 25°C [28]. Brunauer-Emmett-Teller (BET) specific surface area and Barrett-Joyner-Halenda (BJH) pore size distribution were determined by nitrogen adsorption-desorption using a surface area and porosity analyzer (Micromeritics ASAP 2460).

In Vitro ROS Detection and Cytotoxicity Assays

The microwave-driven thermodynamic effect of Zr@C/C NPs was evaluated using the 2',7'-dichlorodihydrofluorescein diacetate (DCFH-DA) fluorescent probe [47]. Hepa1-6 hepatocellular carcinoma cells (purchased from ATCC) were cultured in DMEM supplemented with 10% fetal bovine serum and 1% penicillin-streptomycin at 37°C under 5% CO_2. Cells were seeded in 6-well plates (2×10^5 cells per well) and treated under five conditions: (i) untreated control, (ii) ZrO_2 alone (100 μg mL^{-1}), (iii) Zr@C/C alone (100 μg mL^{-1}), (iv) ZrO_2 + MWA, and (v) Zr@C/C + MWA. For MWA groups, cells were exposed to microwave irradiation (2.45 GHz, 0.9 W, 5 min) using a clinical MWA system (KY-2000, Kangyou Medical). Intracellular ROS levels were quantified by flow cytometry (BD FACSCanto II) after DCFH-DA staining (10 μM, 30 min, 37°C). For apoptosis analysis, cells were harvested 6 h post-treatment, stained with Annexin V-FITC and propidium iodide (PI), and analyzed by flow cytometry [19, 49]. Cell viability was assessed using a CCK-8 assay (Dojindo). Hepa1-6 cells and human umbilical vein endothelial cells (HUVECs) were incubated with Zr@C/C NPs at gradient concentrations (0, 12.5, 25, 50, 100 μg mL^{-1}) for 24 h, and absorbance was measured at 450 nm [15, 18, 46]. All experiments were performed in triplicate.

Rabbit VX2 Liver Tumor Model and MWA Treatment Technique

All animal experiments were approved by the Institutional Animal Care and Use Committee and were conducted in accordance with the institutionally approved animal protocol and reported following the ARRIVE guidelines. New Zealand white rabbits weighing 2.5–3.0 kg (n = 3 per group) were used to establish the VX2 liver tumor model [20]. Briefly, approximately 1 mm^3 VX2 tumor fragments were surgically implanted into the left hepatic lobe adjacent to large blood vessels (> 3 mm in diameter) to reproduce the clinically relevant heat-sink effect [24]. Tumor growth was monitored twice weekly using B-

mode ultrasonography. When the tumor diameter reached 1.0–1.5 cm, the rabbits were randomly allocated to five groups: (i) untreated control, (ii) Zr@C/C nanoparticle monotherapy, (iii) 30-W MWA, (iv) 50-W MWA, and (v) Zr@C/C nanoparticles combined with 30-W MWA. For nanoparticle-treated groups, Zr@C/C nanoparticles were administered intravenously through the marginal ear vein at a dose of 5 mg/kg body weight 24 h before MWA. MWA was performed under real-time ultrasound guidance (LOGIQ E9, GE Healthcare) using a 16-G water-cooled microwave antenna (Kangyou Medical). Ablation was continuously applied for 5 min at the designated power. Contrast-enhanced ultrasonography using Sono Vue (Bracco) was performed at baseline (Day 0, D0) and 24 h after ablation (Day 1, D1) to evaluate the tumor perfusion-defect area [21]. At the predefined experimental endpoint, all rabbits were subjected to the institutionally approved terminal procedure before collection of tumor and peritumoral tissues for histopathological examination (Fig. 1B). Before euthanasia, each rabbit was placed under deep general anesthesia with chloral hydrate at a dose of 100 mg/kg body weight, administered slowly and intravenously through the marginal ear vein. The depth of anesthesia was assessed before proceeding with the terminal procedure. Adequate deep anesthesia was confirmed by complete loss of consciousness, absence of purposeful responses to noxious stimulation, and loss of the corneal reflex, thereby minimizing pain and distress during the terminal procedure. After a deep anesthetic plane had been confirmed, [the actual secondary euthanasia/terminal method used] was performed to ensure irreversible death. Animals were continuously observed throughout the procedure. Death was confirmed by the complete cessation of spontaneous respiration and heartbeat, which remained absent for at least 3 min. Tumor and surrounding liver tissues were collected only after death had been unequivocally confirmed. This terminal procedure was performed according to the protocol approved by the Institutional Animal Care and Use Committee. Deep anesthesia before the terminal procedure was used to ensure that the animals remained unconscious and did not perceive pain or distress during euthanasia and subsequent tissue collection.

Histopathological Analysis

Ablation zone specimens were fixed in 10% neutral buffered formalin, embedded in paraffin, and sectioned at 4 μm thickness. Hematoxylin and eosin (H&E) staining was performed to delineate coagulative necrosis boundaries and assess adjacent vascular integrity [35]. Terminal deoxynucleotidyl transferase dUTP nick end labeling (TUNEL) assay (Roche) was used to detect in situ apoptosis[31, 36]. Immunohistochemistry for Ki67 (1:200, Abcam ab16667) was performed to quantify residual tumor cell proliferation at ablation margins [23, 37]. Stained sections were imaged using a digital slide scanner (Aperio AT2, Leica) and analyzed with ImageJ (NIH).

Statistical Analysis

Data were analyzed using GraphPad Prism 10.0 (GraphPad Software). Continuous variables are presented as mean ± standard deviation (s.d.). Multi-group comparisons were performed by one-way analysis of variance (ANOVA) followed by Tukey's post-hoc test for pairwise comparisons. A two-sided $p < 0.05$ was considered statistically significant. Sample sizes are reported in figure legends. No statistical

method was used to predetermine sample size; group sizes were based on prior experience with the rabbit VX2 model. Blinding was maintained during histopathological scoring.

Results

Synthesis and Physicochemical Characterization of Zr@C/C NPs

The synthetic strategy for Zr@C/C NPs proceeds through three stages: (i) formation of ZrO_2@SiO_2 core-shell structures by hydrolysis and condensation of zirconium (IV) propoxide on silica templates; (ii) selective etching of the SiO_2 core to yield hollow mesoporous ZrO_2 nanospheres; and (iii) vacuum-assisted infiltration of $Cu(NO_3)_2$ followed by solvothermal growth of CuO/Cu-MOF within the interior cavity (Fig. 2A). TEM imaging confirmed that the hollow ZrO_2 [11] nanospheres possess a well-defined spherical morphology with an outer diameter of approximately 160 nm and a shell thickness of approximately 20 nm (Fig. 3B, left). After CuO/Cu-MOF loading [12, 26], the core-shell architecture was preserved, with electron-dense material visible within the interior cavity indicative of successful loading of the copper-based catalytic centers (Fig. 2B, right). Elemental mapping by EDS demonstrated high spatial co-localization of Zr, O, and Cu signals, confirming uniform encapsulation of CuO/Cu-MOF within the ZrO_2 shell (Fig. 2B, mapping panels).

Physicochemical characterization further validated successful synthesis. The hydrated particle size measured by dynamic light scattering (DLS) showed a moderate increase from 195 ± 12 nm (hollow ZrO_2) to 228 ± 15 nm (Zr@C/C NPs), consistent with the loading of CuO/Cu-MOF within the cavity (Fig. 2C) [27, 28]. Zeta potential shifted from − 9.1 ± 1.2 mV (hollow ZrO_2) to − 12.3 ± 1.5 mV (Zr@C/C NPs), indicating surface charge redistribution following CuO/Cu-MOF integration (Fig. 2D) [13, 27]. XRD analysis of Zr@C/C NPs revealed characteristic diffraction peaks of tetragonal ZrO_2 (JCPDS No. 50-1089) at 2θ = 30.2°, 35.2°, 50.4°, and 60.2°, together with additional peaks at 2θ = 35.5° and 38.7° corresponding to the (− 111) and (111) planes of monoclinic CuO (JCPDS No. 48-1548), as well as low-angle peaks consistent with the crystalline framework of Cu-MOF (Fig. 2E) [44]. FTIR spectra of Zr@C/C NPs displayed characteristic absorption bands of the carboxylate groups of H_2BDC at 1580 cm^{-1} (asymmetric stretching) and 1390 cm^{-1} (symmetric stretching), along with Cu-O stretching vibrations at 530 cm^{-1}, confirming successful coordination of the Cu-MOF structure (Fig. 2F) [16]. Collectively, these results confirm the successful construction of a hollow mesoporous ZrO_2 nanoplatform with uniformly loaded CuO/Cu-MOF catalytic centers.

In Vitro ROS Generation and Antitumor Efficacy Under Simulated Heat-Sink Conditions

We evaluated the ROS-generating capacity and tumor-cell-killing efficacy of Zr@C/C NPs under simulated heat-sink conditions in vitro. Cells were incubated with NPs (100 μg mL^{-1}) and exposed to microwave irradiation at a sublethal temperature (41 ~ 43°C) to mimic the perivascular zone where thermal energy is insufficient to induce coagulative necrosis. Flow cytometry using DCFH-DA revealed that the Zr@C/C + MWA group produced a 7.8-fold increase in mean DCF fluorescence intensity

compared to the untreated control, significantly higher than that of the ZrO_2 + MWA group (2.4-fold, $p < 0.001$) and all non-irradiated groups (Fig. 3B). This pronounced ROS burst is attributed to microwave-triggered catalytic activity of the CuO/Cu-MOF centers [32].

Apoptosis analysis by Annexin V-FITC/PI flow cytometry demonstrated that the Zr@C/C + MWA treatment induced 62.4 ± 4.1% total apoptosis (early + late), compared with 18.6 ± 2.3% in the ZrO_2 + MWA group and < 8% in all control groups (Fig. 3A, C; $p < 0.001$). These results confirm that the CuO/Cu-MOF catalytic centers convert microwave energy into ROS-mediated cytotoxicity, effectively compensating for the physical thermal deficit within the sublethal temperature range.

The CCK-8 assay showed that Zr@C/C NPs exhibited minimal intrinsic cytotoxicity. HEK-293 and HUVEC cell viability remained above 77.5% at the highest tested concentration (100 μg mL^{-1}) after 24 h co-incubation (Fig. 3F, G) [46], indicating that the hollow ZrO_2 shell effectively confines the copper-based catalytic species and limits off-target toxicity. In contrast, under MWA irradiation, Zr@C/C NPs produced a significant concentration-dependent reduction in Hepa1-6 cell viability, reaching 61.8 ± 3.5% cell death at 100 μg mL^{-1}, whereas hollow ZrO_2 alone produced only minimal cytotoxicity under identical conditions (Fig. 3D, E) [18].

In Vivo MWA Efficacy in a Rabbit VX2 Perivascular Liver Tumor Model

To evaluate the translational relevance of Zr@C/C NPs, we established a rabbit VX2 liver tumor model with tumors implanted adjacent to major hepatic vessels to recapitulate the clinical heat-sink effect [24, 48]. Real-time intraoperative ultrasound confirmed accurate antenna placement and enabled dynamic monitoring of the hyperechoic ablation zone during MWA (Fig. 4B) [33, 34]. CEUS performed at 24 h post-ablation revealed persistent perfusion at the vascular margins in the conventional MWA group (50 W), consistent with incomplete ablation due to convective heat dissipation. In contrast, the Zr@C/C + MWA (30 W) group achieved complete non-perfusion zones with sharply demarcated ablation boundaries (Fig. 4A, C). Quantitative analysis of CEUS images confirmed a significantly larger non-perfused volume in the Zr@C/C + MWA (30 W) group (4.18 ± 0.35 cm^3) compared to the MWA-only group at 50 W (2.06 ± 0.22 cm^3, $p < 0.01$), despite the lower applied power [21].

Histopathological evaluation corroborated the CEUS findings. H&E staining revealed extensive, well-demarcated coagulative necrosis in the Zr@C/C + MWA group, with clear transition zones between ablated and viable tissue (Fig. 4D) [35]. Critically, adjacent large vessels remained structurally intact, with preserved endothelial lining and no evidence of thermal thrombotic occlusion. TUNEL staining demonstrated dense, uniformly distributed apoptotic signals within the perivascular sublethal zone of the Zr@C/C + MWA group, whereas the conventional MWA group exhibited sparse TUNEL-positive cells confined to the immediate needle tract (Fig. 4E, 4A) [36]. Quantitative analysis confirmed a 3.2-fold higher TUNEL-positive cell density in the Zr@C/C + MWA group ($p < 0.001$). Ki67 immunohistochemistry showed a marked reduction in the tumor proliferation index at ablation margins in the Zr@C/C + MWA group (8.3 ± 2.1%) compared to the MWA-only group (29.6 ± 4.2%, $p < 0.01$, Fig. 5B) [37]. These results

collectively demonstrate that Zr@C/C NPs enhance MWA efficacy by generating ROS-mediated cytotoxicity within the heat-sink zone, achieving complete tumor inactivation at reduced power while preserving adjacent vascular structures [38, 49].

Discussion

This study demonstrates that CuO/Cu-MOF-loaded hollow mesoporous ZrO_2 nanospheres function as effective microwave-responsive sensitizers, addressing two long-standing limitations of MWA for HCC: incomplete ablation at vascular margins and collateral thermal injury. The key finding is that Zr@C/C NPs, by converting sublethal microwave energy into ROS-mediated cytotoxicity, enable equivalent or superior tumor ablation at 30 W compared to conventional MWA at 50 W, thereby narrowing the gap between oncological efficacy and procedural safety [39].

The physicochemical characterization confirms that the hollow architecture of Zr@C/C NPs serves a dual function. The ZrO_2 shell provides a thermally stable dielectric scaffold that enhances microwave absorption through multiple internal reflections [42], while the interior cavity accommodates CuO/Cu-MOF catalytic centers at high loading capacity [41]. This spatial segregation—catalytic centers confined within a biocompatible shell—explains the favorable toxicity profile observed in vitro: Zr@C/C NPs exhibited minimal cytotoxicity toward normal HUVEC and HEK-293 cells even at high concentrations, consistent with effective physical containment of the copper species [30].

Under microwave irradiation, the CuO/Cu-MOF centers generate ROS through a combination of mechanisms, including microwave-induced electron-hole pair generation in CuO and Fenton-like catalytic cycling of Cu^{2+}/Cu^{+} at the Cu-MOF nodes [32]. This ROS burst augments the physical thermal effect of MWA within the sublethal temperature zone (40–45°C), where heat alone is insufficient to induce coagulative necrosis [47]. The in vivo data from the rabbit VX2 perivascular tumor model provide direct evidence for this "thermal-kinetic" mechanism: TUNEL-positive apoptotic cells were concentrated in the perivascular region, where convective heat dissipation by blood flow would be expected to produce the greatest thermal deficit [20]. The preservation of adjacent vascular integrity—confirmed by H&E staining and the absence of thrombotic occlusion—is particularly noteworthy, as it suggests that the reduction in required microwave power directly translates into reduced collateral thermal damage [24].

Several limitations of this study should be acknowledged. First, the in vivo evaluation was conducted exclusively in the rabbit VX2 model. Although this model effectively replicates the perivascular heat-sink effect, differences in liver anatomy, vascular architecture, and tumor microenvironment between rabbits and humans necessitate validation in large-animal models—such as porcine liver—before clinical translation can be considered [22, 39]. Second, the molecular signaling pathways mediating ROS-induced apoptosis (e.g., caspase-dependent and MAPK pathways) were not investigated; systematic dissection of these cascades would strengthen the mechanistic framework [8, 9, 19]. Third, the current tumor accumulation of Zr@C/C NPs relies primarily on the enhanced permeability and retention (EPR) effect,

which is inherently heterogeneous. Surface functionalization with active targeting ligands could improve tumor specificity and therapeutic index [14]. Fourth, the long-term biodistribution, metabolic clearance, and chronic toxicity profile of Zr@C/C NPs require comprehensive evaluation over extended observation periods [39]. Addressing these questions will be essential for advancing this platform toward clinical application [38].

Conclusion

We have developed CuO/Cu-MOF-loaded hollow mesoporous ZrO_2 nanospheres (Zr@C/C NPs) as a microwave-responsive sensitizer for HCC ablation. The key design principle is the spatial segregation of microwave-responsive CuO/Cu-MOF catalytic centers within a biocompatible hollow ZrO_2 scaffold, which enables efficient conversion of sublethal microwave energy into ROS-mediated cytotoxicity. In vitro, Zr@C/C NPs under microwave irradiation generated a pronounced ROS burst and induced substantial apoptosis in Hepa1-6 cells at sublethal temperatures, without intrinsic cytotoxicity. In a rabbit VX2 perivascular liver tumor model, Zr@C/C NP-mediated MWA at 30 W achieved greater coagulative necrosis and more effective tumor control than conventional MWA at 50 W, while preserving adjacent vascular structures. These results provide a preclinical rationale for the "thermal-kinetic" strategy as a means of reconciling MWA efficacy with procedural safety. Further studies in large-animal models and comprehensive long-term safety evaluation are warranted to establish the translational potential of this approach [38].

Abbreviations

MWA	Microwave ablation
HCC	Hepatocellular carcinoma
Zr@C/C NPs	CuO/Cu-metal–organic frameworks
ROS	Reactive oxygen species
ZrO_2	Zirconium dioxide
EDS	Energy-dispersive X-ray spectroscopy
FTIR	Fourier transform infrared
BET	Brunauer-Emmett-Teller
BJH	Barrett-Joyner-Halenda
PI	Propidium iodide
MDT	Microwave dynamic therapy

CEUS Contrast-enhanced ultrasound

Declarations

Ethics approval and consent to participate

The animal experiment was authorized according to the Chongqing Medical University Animal Care guidelines.

Consent for publication

Not applicable.

Competing interests

Conflict of Interest Statement: All authors of this paper declare that there are no conflicts of interest and no potential interest relationships that could affect the objectivity and impartiality of this study.

Author details

[1]Chongqing Key Laboratory of Ultrasound Molecular Imaging &Department of Ultrasound, Second Affiliated Hospital of Chongqing Medical University

[2]Chinese PLA General Hospital, Beijing, China

First author: Xiu-Xiu Hao[1, 2]*, Address: The Fifth Medical Center of Chinese PLA General Hospital, No.8 East Street, Fengtai District, Beijing, China

First corresponding author: Hai-Tao Ran Chongqing Key Laboratory of Ultrasound Molecular Imaging &

Department of Ultrasound, Second Affiliated Hospital of Chongqing

Medical University, No. 74 Linjiang Rd, Yuzhong District,

Chongqing 400010, Email: ranhaitao@cqmu.edu.cn

Ping Liang and Hai-Tao Ran contribute equally as co-corresponding authors of this work.

Funding

This work was supported by the National Natural Science Foundation of China under Grant No. 82572233, Project Name: Research on the Mechanism of Ultrasound-Regulated Stem Cell-Derived β-Cell Function and Treatment of Type 1 Diabetes

Author Contribution

Haitao Ran Ping Liang designed the experiment and reviewed the manuscript.Liting He ,Xiuxiu Hao and Jie Zhou prepared figures 1-5. Xiuxiu Hao ,Wei Zhang, Yun Zhou, Jie Zhou ,Run-Min Zha, Mao Tang, made the experimental operation and data collation.Wei Zhang, Xiuxiu Hao ,Liting He, Yun Zhou,Run-Min Zha, Ming-Yuan Dai processed the data.Liting He, Xiuxiu Hao ,Ming-Yuan Dai analysed the experimental data.Xiuxiu Hao wrote the main manuscript text.

Data Availability

All data generated or analyzed during the present study are included in this manuscript.

References

1. Lin X, Chen S, Su Y, Wu Y, Huang L, Ye Q, Song J. Ultrasound activated nanobowls with deep penetration for enhancing sonodynamic therapy of orthotopic liver cancer. Adv Sci. 2024;11(13):e2306301. https://doi.org/10.1002/advs.202306301. . PMID: 38247202; PMCID: PMC10987158.
2. Zhou H, Liu Z, Zhang Z, Pandey NK, Amador E, Nguyen W, Chudal L, Xiong L, Chen W, Wen Y. Copper-cysteamine nanoparticle-mediated microwave dynamic therapy improves cancer treatment with induction of ferroptosis. Bioact Mater. 2023;24:322–30. https://doi.org/10.1016/j.bioactmat.2022.12.023. . PMID: 36632507; PMCID: PMC9807746.
3. Pomponio R, Tang Q, Mei A, Caron A, Coulibaly B, Theilhaber J, Rogers-Grazado M, Sanicola-Nadel M, Naimi S, Olfati-Saber R, Combeau C, Pollard J, Lin TT, Wang R. An integrative approach of digital image analysis and transcriptome profiling to explore potential predictive biomarkers for TGFβ blockade therapy. Acta Pharm Sin B. 2022;12(9):3594–601. https://doi.org/10.1016/j.apsb.2022.03.013. . PMID: 36176910; PMCID: PMC9513441.
4. Cui R, Wang L, Zhang D, Zhang K, Dou J, Dong L, Zhang Y, Wu J, Tan L, Yu J, Liang P. Combination therapy using microwave ablation and d-mannose-chelated iron oxide nanoparticles inhibits hepatocellular carcinoma progression. Acta Pharm Sin B. 2022;12(9):3475–85. https://doi.org/10.1016/j.apsb.2022.05.026. . PMID: 36176908; PMCID: PMC9513490.
5. Zhang J, Sun X, Zhao X, Yang C, Shi M, Zhang B, Hu H, Qiao M, Chen D, Zhao X. Combining immune checkpoint blockade with ATP-based immunogenic cell death amplifier for cancer chemo-immunotherapy. Acta Pharm Sin B. 2022;12(9):3694–709. https://doi.org/10.1016/j.apsb.2022.05.008. . PMID: 36176905; PMCID: PMC9513492.
6. Chen X, Fan X, Zhang Y, Wei Y, Zheng H, Bao D, Xu H, Piao JG, Li F, Zheng H. Cooperative coordination-mediated multi-component self-assembly of all-in-one nanospike theranostic nano-platform for MRI-guided synergistic therapy against breast cancer. Acta Pharm Sin B.

2022;12(9):3710–25. https://doi.org/10.1016/j.apsb.2022.02.027. . PMID: 36176903; PMCID: PMC9513557.

7. Mao X, Wang X, Jin M, Li Q, Jia J, Li M, Zhou H, Liu Z, Jin W, Zhao Y, Luo Z. Critical involvement of lysyl oxidase in seizure-induced neuronal damage through ERK-Alox5-dependent ferroptosis and its therapeutic implications. Acta Pharm Sin B. 2022;12(9):3513–28. https://doi.org/10.1016/j.apsb.2022.04.017. . PMID: 36176900; PMCID: PMC9513491.
8. Li F, Lai Y, Ye J, Saeed M, Dang Y, Zou Z, Chen F, Zhang W, Xu Z. Dual-targeting prodrug nanotheranostics for NIR-Ⅱ fluorescence imaging-guided photoimmunotherapy of glioblastoma. Acta Pharm Sin B. 2022;12(9):3486–97. https://doi.org/10.1016/j.apsb.2022.05.016. . PMID: 36176914; PMCID: PMC9513488.
9. Guan S, Chen X, Chen Y, Wan G, Su Q, Liang H, Yang Y, Fang W, Huang Y, Zhao H, Zhuang W, Liu S, Wang F, Feng W, Zhang X, Huang M, Wang X, Zhang L. FOXO3 mutation predicting gefitinib-induced hepatotoxicity in NSCLC patients through regulation of autophagy. Acta Pharm Sin B. 2022;12(9):3639–49. https://doi.org/10.1016/j.apsb.2022.02.006. . PMID: 36176901; PMCID: PMC9513443.
10. Wang F, Li Z, Chen L, Yang T, Liang B, Zhang Z, Shao J, Xu X, Yin G, Wang S, Ding H, Zhang F, Zheng S. Inhibition of ASCT2 induces hepatic stellate cell senescence with modified proinflammatory secretome through an IL-1α/NF-κB feedback pathway to inhibit liver fibrosis. Acta Pharm Sin B. 2022;12(9):3618–38. https://doi.org/10.1016/j.apsb.2022.03.014. . PMID: 36176909; PMCID: PMC9513497.
11. Gu Y, Wang R, Chen P, Li S, Chai X, Chen C, Liu Y, Cao Y, Lv D, Hong Z, Zhu Z, Chai Y, Yuan Y, Chen X. In situ synthesis and unidirectional insertion of membrane proteins in liposome-immobilized silica stationary phase for rapid preparation of microaffinity chromatography. Acta Pharm Sin B. 2022;12(9):3682–93. https://doi.org/10.1016/j.apsb.2022.04.010. . PMID: 36176904; PMCID: PMC9513493.
12. Sun J, Jin T, Niu Z, Guo J, Guo Y, Yang R, Wang Q, Gao H, Zhang Y, Li T, He W, Li Z, Ma W, Su W, Li L, Fan X, Shan H, Liang H. LncRNA DACH1 protects against pulmonary fibrosis by binding to SRSF1 to suppress CTNNB1 accumulation. Acta Pharm Sin B. 2022;12(9):3602–17. https://doi.org/10.1016/j.apsb.2022.04.006. . PMID: 36176913; PMCID: PMC9513499.
13. Wu H, Yao H, He C, Jia Y, Zhu Z, Xu S, Li D, Xu J. Molecular glues modulate protein functions by inducing protein aggregation: a promising therapeutic strategy of small molecules for disease treatment. Acta Pharm Sin B. 2022;12(9):3548–66. https://doi.org/10.1016/j.apsb.2022.03.019. . PMID: 36176907; PMCID: PMC9513498.
14. Chen X, Zou Y, Zhang S, Fang P, Li S, Li P, Sun Y, Yuan G, Hu H. Multifunctional vesicles improve Helicobacter pylori eradication by a comprehensive strategy based on complex pathological microenvironment. Acta Pharm Sin B. 2022;12(9):3498–512. https://doi.org/10.1016/j.apsb.2022.05.014. . PMID: 36176916; PMCID: PMC9513559.

15. Wang X, Hua P, He C, Chen M. Non-apoptotic cell death-based cancer therapy: molecular mechanism, pharmacological modulators, and nanomedicine. Acta Pharm Sin B. 2022;12(9):3567–93. https://doi.org/10.1016/j.apsb.2022.03.020. . PMID: 36176912; PMCID: PMC9513500.
16. Miao L, Zhou W, Yan C, Zhang Y, Qiao Q, Zhou X, Chen Y, Wang G, Guo Z, Liu J, Piao H, Pan X, Yan M, Zhao W, Li G, Li Y, Xu Z. Rapid screening of SARS-CoV-2 inhibitors via ratiometric fluorescence of RBD-ACE2 complexes in living cells by competitive binding. Acta Pharm Sin B. 2022;12(9):3739–42. https://doi.org/10.1016/j.apsb.2022.05.033. . PMID: 35693447; PMCID: PMC9167803.
17. Cen X, Wang B, Liang Y, Chen Y, Xiao Y, Du S, Nandakumar KS, Yin H, Liu S, Cheng K. Small molecule SMU-CX24 targeting toll-like receptor 3 counteracts inflammation: a novel approach to atherosclerosis therapy. Acta Pharm Sin B. 2022;12(9):3667–81. https://doi.org/10.1016/j.apsb.2022.06.001. . PMID: 36176917; PMCID: PMC9513496.
18. Tong J, Li D, Meng H, Sun D, Lan X, Ni M, Ma J, Zeng F, Sun S, Fu J, Li G, Ji Q, Zhang G, Shen Q, Wang Y, Zhu J, Zhao Y, Wang X, Liu Y, Ouyang S, Sheng C, Shen F, Wang P. Targeting a novel inducible GPX4 alternative isoform to alleviate ferroptosis and treat metabolic-associated fatty liver disease. Acta Pharm Sin B. 2022;12(9):3650–66. https://doi.org/10.1016/j.apsb.2022.02.003. . PMID: 36176906; PMCID: PMC9513461.
19. Ji L, Li Q, He Y, Zhang X, Zhou Z, Gao Y, Fang M, Yu Z, Rodrigues RM, Gao Y, Li M. Therapeutic potential of traditional Chinese medicine for the treatment of NAFLD: a promising drug Potentilla discolor Bunge. Acta Pharm Sin B. 2022;12(9):3529–47. https://doi.org/10.1016/j.apsb.2022.05.001. . PMID: 36176915; PMCID: PMC9513494.
20. Zhang W, Zhang C, Yang C, Wang X, Liu W, Yang M, Cao Y, Ran H. Photochemically-driven highly efficient intracellular delivery and light/hypoxia programmable triggered cancer photochemotherapy. J Nanobiotechnol. 2023;21(1):11. https://doi.org/10.1186/s12951-023-01774-w. . PMID: 36631855; PMCID: PMC9835365.
21. Ouyang J, Xie A, Zhou J, Liu R, Wang L, Liu H, Kong N, Tao W. Minimally invasive nanomedicine: nanotechnology in photo-/ultrasound-/radiation-/magnetism-mediated therapy and imaging. Chem Soc Rev. 2022;51(12):4996–5041. https://doi.org/10.1039/d1cs01148k. PMID: 35616098.
22. Zhao PH, Wu YL, Li XY, Feng LL, Zhang L, Zheng BY, Ke MR, Huang JD. Aggregation-enhanced sonodynamic activity of phthalocyanine-artesunate conjugates. Angew Chem Int Ed. 2022;61(5):e202113506. https://doi.org/10.1002/anie.202113506. PMID: 34761489.
23. Wang D, Lin L, Li T, Meng M, Hao K, Guo Z, Chen J, Tian H, Chen X. Etching bulk covalent organic frameworks into nanoparticles of uniform and controllable size by the molecular exchange etching method for sonodynamic and immune combination antitumor therapy. Adv Mater. 2022;34(45):e2205924. https://doi.org/10.1002/adma.202205924. PMID: 36039617.
24. Mundhava M, Vadodariya B, Jangid P, Shah A. Histotripsy compared with microwave ablation, radiofrequency ablation, and stereotactic body radiotherapy for the treatment of liver tumors. Cureus. 2025;17(12):e100088. https://doi.org/10.7759/cureus.100088. . PMID: 41458348; PMCID: PMC12741011.

25. Wu MS, Kao WY, Chiang MF, Chuang PH, Hsu SJ, Wang SY, Chang CW, Lin CC, Hung CH, Wu CH, Chen SC, Lee HL, Hwang JI, Liang PC, Lin SM, Wang CC. Consensus guideline of ablation for metastatic liver tumors by Taiwan Academy of Tumor Ablation. Liver Cancer. 2025;15(1):149–64. https://doi.org/10.1159/000546765. . PMID: 40686658; PMCID: PMC12270489.
26. Arik E, Taydas O, Dertli T, Sevinc OF, Kara AB, Topaloglu OF, Ozdemir M, Senturk A, Canturk AO, Hacibekiroglu I, Ozturk MH. Efficacy and safety of percutaneous microwave ablation for liver tumors using an antenna with anti-phase technology offering ultraspherical ablation. Radiol Oncol. 2025;59(4):526–34. https://doi.org/10.2478/raon-2025-0064. . PMID: 41401063; PMCID: PMC12707445.
27. van Erp GCM, Verdonschot KHM, Broersen A, Hendriks P, Overduin CG, Dijkstra J, Burgmans MC. Percutaneous microwave ablation of liver tumors: predicted versus actual ablation zones. Int J Hyperthermia. 2026;43(1):2683504. https://doi.org/10.1080/02656736.2026.2683504. PMID: 42338223.
28. Yang W, Li X, Tan X. Microwave ablation versus radiofrequency ablation for hepatocellular carcinoma: a propensity score matching and inverse probability weighting analysis. Int J Hyperthermia. 2025;42(1):2524389. https://doi.org/10.1080/02656736.2025.2524389. PMID: 40665719.
29. Wang Q, Wu S, Li L, Xue X, Zhang H, Wu W, Gao H. Personalized simulation modeling of overlapping microwave ablation for large tumors. Bioengineering. 2026;13(4):421. https://doi.org/10.3390/bioengineering13040421. . PMID: 42072215; PMCID: PMC13113720.
30. Liu H, Fan Z, Zhang R, Zhang X, Wang J. Combined therapy with microwave ablation and conventional transarterial chemoembolization for hepatocellular carcinoma tumors larger than five centimetres: a prospective study. Diagn Interv Radiol. 2026;32(1):96–103. https://doi.org/10.4274/dir.2025.253308. . PMID: 40622188; PMCID: PMC12766349.
31. Demir M, Avci MT, Agackiran A, Emir S, Acar A, Canbak T. Microwave ablation for hepatocellular carcinoma: a single-center experience and outcomes. North Clin Istanb. 2025;12(6):700–6. https://doi.org/10.14744/nci.2025.34101. . PMID: 41574135; PMCID: PMC12821121.
32. Zhang L, Ngu A, Kupke LS, Mayr V, Strotzer Q, Brandenstein M, Stroszczynski C, Einspieler I. Combined single-session stereotactic biopsy and microwave ablation of primary and secondary liver tumors. Biomedicines. 2025;13(12):2865. https://doi.org/10.3390/biomedicines13122865. . PMID: 41462880; PMCID: PMC12730351.
33. Bahloul C, Rode A, Pradat P, Milot L, Dumortier J, Merle P, Mabrut JY, Boussel L, Della Corte A. Multibipolar radiofrequency vs single needle microwave ablation for the treatment of newly diagnosed hepatocellular carcinoma. World J Gastroenterol. 2026;32(2):113810. https://doi.org/10.3748/wjg.v32.i2.113810. . PMID: 41551836; PMCID: PMC12809236.
34. Yan H, Xiong H, Zhou H, Zhou C. Hepatectomy outperforms microwave ablation for colorectal cancer liver metastases, with anatomical location affecting ablation outcomes. Front Surg.

2026;13:1878151. https://doi.org/10.3389/fsurg.2026.1878151. . PMID: 42548666; PMCID: PMC13429659.

35. Soukar J, Singh KA, Aviles A, Hargett S, Kaur H, Foster S, Roy S, Zhao F, Gohil VM, Singh I, Gaharwar AK. Nanomaterial-induced mitochondrial biogenesis enhances intercellular mitochondrial transfer efficiency. Proc Natl Acad Sci U S A. 2025;122(43):e2505237122. https://doi.org/10.1073/pnas.2505237122. . PMID: 41134634; PMCID: PMC12582283.
36. Sang W, Fan H, Huang Y, Zhang J, Gao W, Zhao C, Liu X, Zhao L, Liu Y, Dai Y, Zhang R. New strategies for tumor diagnosis and therapy with ultrasound assisted by nanomaterials. Ultrason Sonochem. 2025;121:107542. https://doi.org/10.1016/j.ultsonch.2025.107542. . PMID: 40926449; PMCID: PMC12454903.
37. Krishnan N, Jiang Y, Zhou J, Mohapatra A, Peng FX, Duan Y, Holay M, Chekuri S, Guo Z, Gao W, Fang RH, Zhang L. A modular approach to enhancing cell membrane-coated nanoparticle functionality using genetic engineering. Nat Nanotechnol. 2024;19(3):345–53. https://doi.org/10.1038/s41565-023-01533-w. . PMID: 37903891; PMCID: PMC10954421.
38. Melaibari AA, Basem A, Al-Bonsrulah HAZ, Alazwari MA, Abu-Hamdeh NH. Numerical investigation of radiation-assisted freezing in nanomaterial-enhanced porous enclosures. Sci Rep. 2026;16(1):23553. https://doi.org/10.1038/s41598-026-62012-5. . PMID: 42449142; PMCID: PMC13421501.
39. Huang L, Fu Y, Li F. Nanomaterial-enhanced corneal cross-linking: engineering strategies for transforming keratoconus management. Pharmaceutics. 2026;18(7):778. https://doi.org/10.3390/pharmaceutics18070778. . PMID: 42514859; PMCID: PMC13416406.
40. Darvishi M, Heidari MM, Kheradmand R, Niaki NM, Tabean M, Mobed A. Nanomaterial-enhanced electrochemical sensors for clinical monitoring of acyclovir: integration into molecular diagnostics. J Clin Lab Anal. 2025;39(20):e70104. https://doi.org/10.1002/jcla.70104. . PMID: 41025254; PMCID: PMC12572734.
41. Liu ZL, Lu Q, Zhang Q, Fan WW, Chen J, Liu LP. NAFLD accelerates arterial perfusion in rabbit VX2 liver tumors: a sonoVue-based contrast-enhanced ultrasound study. Front Oncol. 2025;15:1638869. https://doi.org/10.3389/fonc.2025.1638869. . PMID: 40994954; PMCID: PMC12454042.
42. Yuan G, Cui R, Xu Y, Luo J, Zheng B, Hu W, Zhang X, Si G. Comparing minimally invasive puncture under local anesthesia to open laparotomy under general anesthesia for establishing a rabbit VX2 liver tumor model. J Hepatocell Carcinoma. 2026;13:588361. https://doi.org/10.2147/JHC.S588361. . PMID: 41710698; PMCID: PMC12912104.
43. Yang T, Zhu X, Tang F, Wu X, Chen J, Li F, Li H, Xiang X, Duan X, Ren J, Chen P. Pharmacokinetics and anti-tumor efficacy of transarterial chemoembolization using small-particle lenvatinib-loaded beads in a rabbit VX2 liver tumor model. Quant Imaging Med Surg. 2026;16(6):495. https://doi.org/10.21037/qims-2025-aw-2277. . PMID: 42273140; PMCID: PMC13247929.
44. Li Y, Chen J, Zhang J, Li Z, Zhang Y, Chen H, Zhou B, Yao Y, Ren K, Liu X. Temperature-sensitive liquid embolic agent loaded with Lobaplatin in the TACE procedure for rabbit VX2 liver tumor. Sci Rep.

2026; https://doi.org/10.1038/s41598-026-54052-8. PMID: 42177322.

45. Li L, Xie W, Sun H, Yu H, Wang C, Zheng M, Shi P, Tian H, Xiong T. Synergistic effect of doxorubicin-thermo-iodized oil pickering emulsions on the interventional embolization-chemotherapy-immunity of VX2 rabbit liver cancer. Int J Nanomed. 2026;21:569851. https://doi.org/10.2147/IJN.S569851. . PMID: 42220971; PMCID: PMC13221567.
46. Xu X, Zhao Z, Wang Y, Liu Z, Liu Z, Li X, Mao Z, Xu L, Lin G, Liu G, Ma H. Ultra-radiostable covalent conformationally interlocked networks enabling a universal radiometal-labeling platform for cancer radioembolization. Adv Sci. 2026;e76278. https://doi.org/10.1002/advs.76278. . PMID: 42335402; PMCID: PMC13336425.
47. Du N, Zhang W, Chen C, Wang Y, He X, Luo J, Yan Z, Li WT. Sequential and synergistic delivery of lipiodol and drug-eluting microspheres circumvents incompatibility to enhance targeted chemoembolization. Front Pharmacol. 2026;17:1800481. https://doi.org/10.3389/fphar.2026.1800481. . PMID: 41982674; PMCID: PMC13071007.
48. Westby K, Westby D, McKevitt K, Moloney BM. Artificial intelligence in thermal ablation: current applications and future directions in microwave technologies. Biomimetics. 2025;10(12):818. https://doi.org/10.3390/biomimetics10120818. . PMID: 41439886; PMCID: PMC12730249.
49. Dong TT, Li M, Li YY, Yin C, Nie F. Prediction of tumor progression after microwave ablation of hepatocellular carcinoma by contrast-enhanced ultrasound combined with immunohistochemical markers. J Hepatocell Carcinoma. 2026;13:539184. https://doi.org/10.2147/JHC.S539184. . PMID: 41773234; PMCID: PMC12949801.

Figures

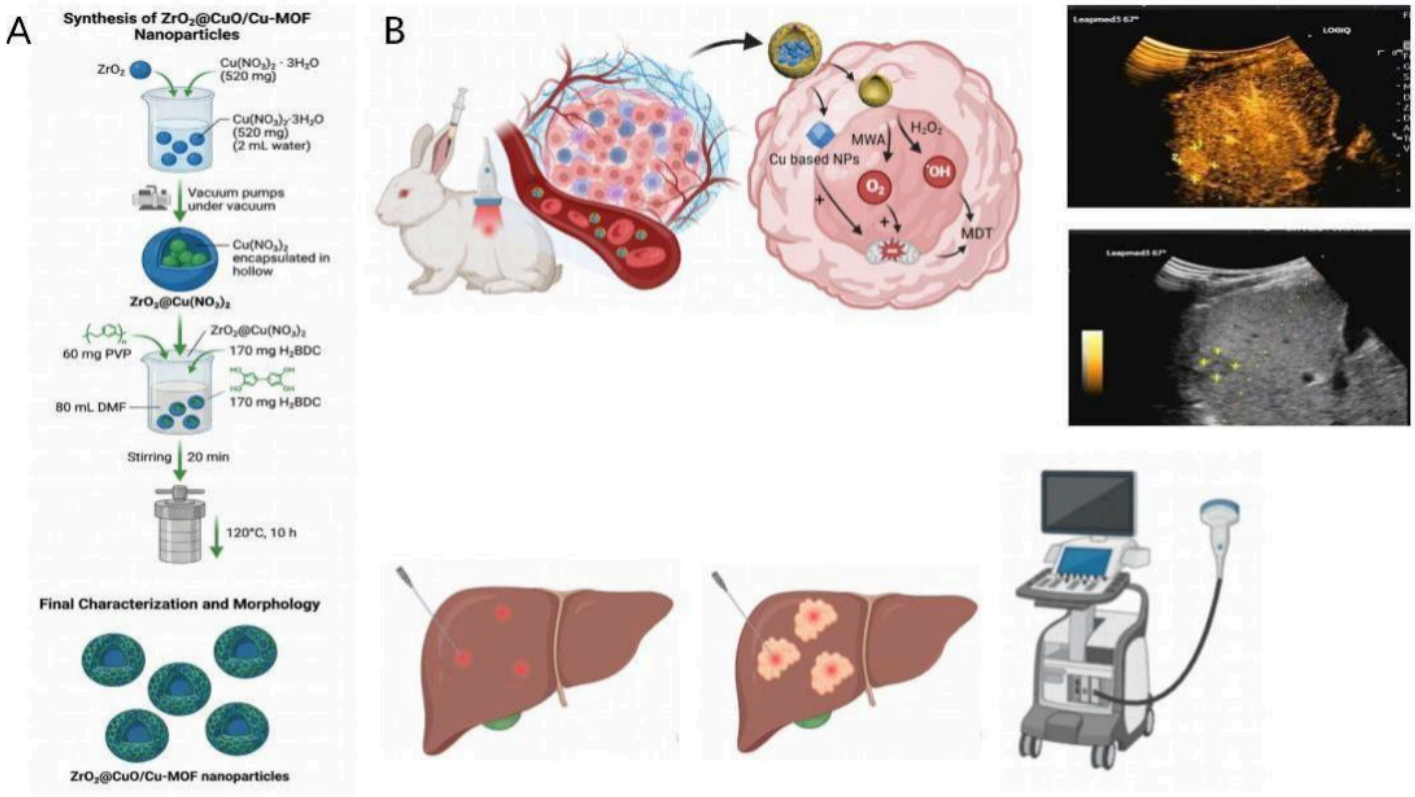


Figure 1

Schematic representation of the study workflow(A) Schematic illustration of the synthesis of Zr@APC/C nanoparticles.(B) Schematic representation (not drawn to scale) of Zr@APC/C nanoparticles generating oxygen to boost ROS production, which is utilized for enhanced microwave dynamic therapy and antiangiogenesis under microwave radiation.

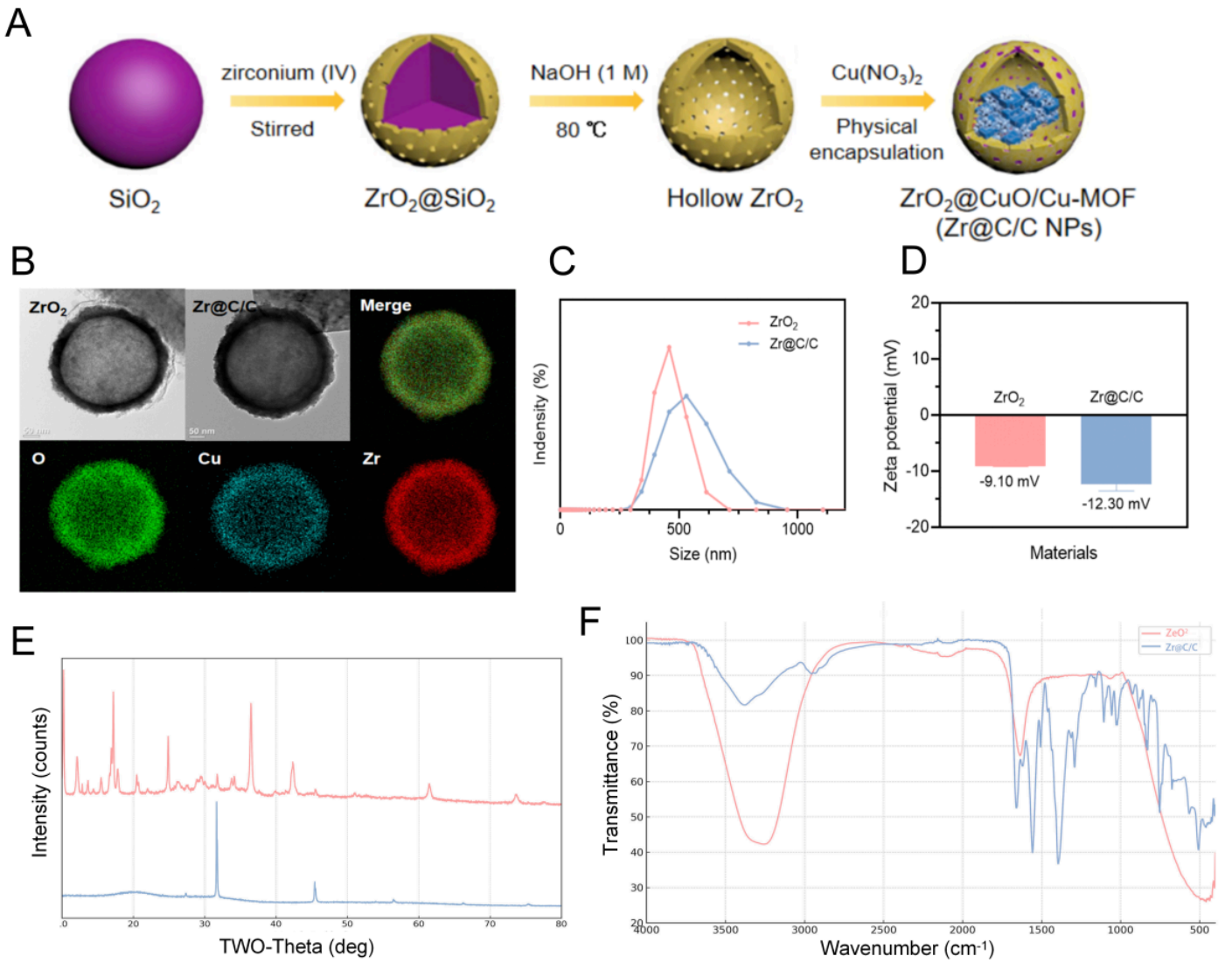


Figure 2

Synthesis and characterization of Zr@C/CNPs. (A)Schematic Diagram of the Synthetic Route: Illustrates the preparation procedure involving the use of SiO_2 as a template, coating with a ZrO_2 shell, alkali etching to form a hollow structure, and subsequent physical encapsulation of $Cu(NO_3)_2$.(B) TEM morphology characterization and element distribution map (Mapping): Transmission electron micrographs of hollow ZrO_2 nanospheres and Zr@C/C nanoparticles, showing a clear core-shell structure and the distribution of active centers in the cavity. Elemental mapping analysis of Zr@C/C nanoparticles (Merge, O, Cu, Zr) confirms that copper-based active components are successfully loaded in the hollow cavity of zirconium dioxide.(C) Zeta potential analysis: The change in surface charge between ZrO_2 (-9.10 mV) and Zr@C/C (-12.30 mV) was compared, reflecting the successful modification of the material surface.(D) Particle size distribution map (DLS): Hydrated particle size distribution curves of ZrO_2 and Zr@C/C nanoparticles measured by dynamic light scattering.(E) XRD diffraction pattern: X-ray diffraction analysis of the material confirms the presence of ZrO_2 and Zr@C/C crystal phases in the nanoplatform.(F) FTIR infrared

spectrum: Fourier transform infrared spectroscopy analysis shows the functional group information on the material surface and the successful loading of organic ligands.

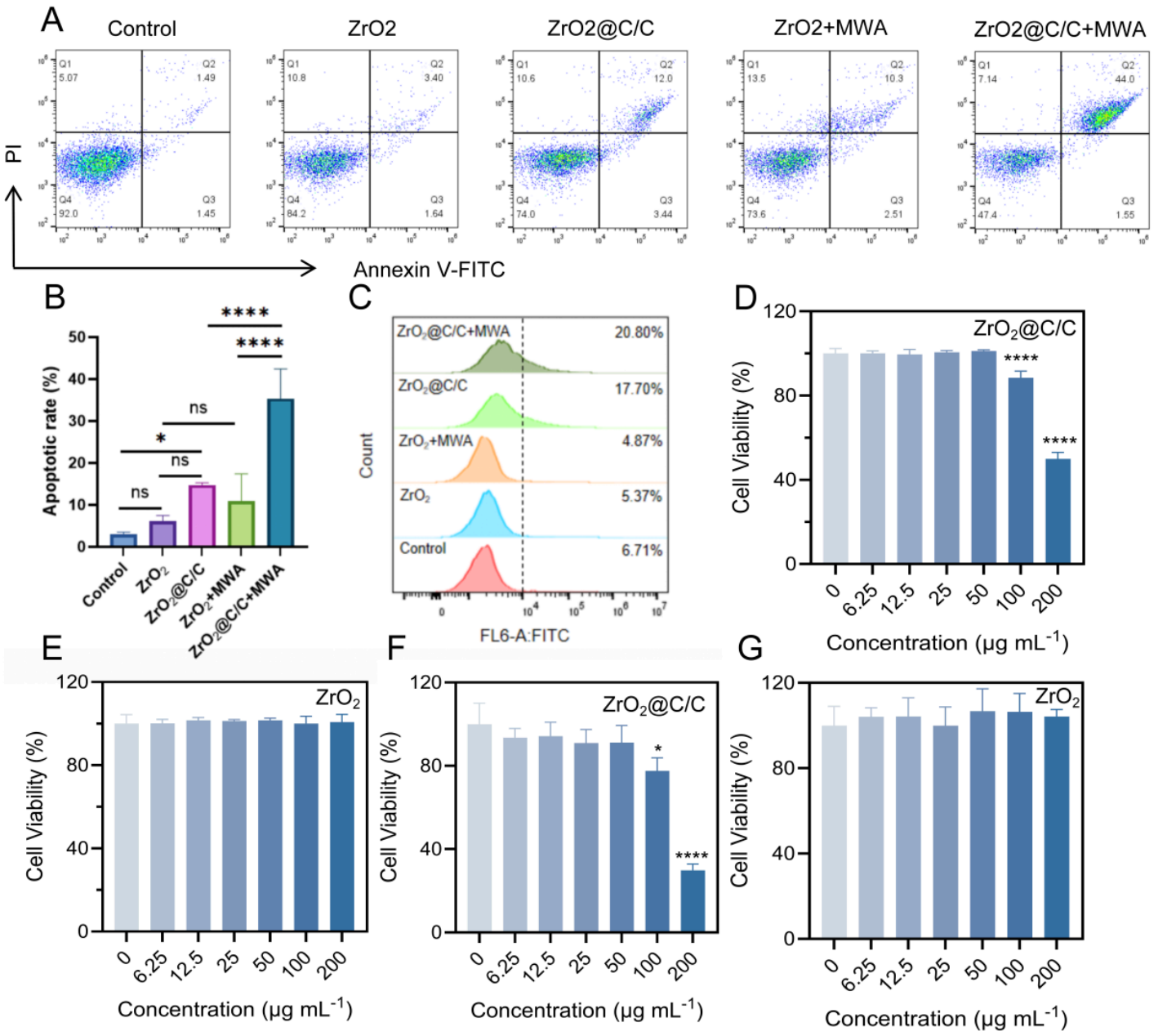


Figure 3

In vitro evaluation of Zr@C/CNPs.(A) Flow cytometry of tumor cell apoptosis under different treatment groups and (B) quantitative analysis: Quantitative analysis of the effect of inducing apoptosis in hepatocellular carcinoma cells by different treatment groups (Control, ZrO_2, ZrO_2@C/C, ZrO_2+MWA, ZrO_2@C/C+MWA), showing that the apoptosis rate in the experimental groups was significantly increased.(C) Flow cytometry detection of intracellular ROS levels: The levels of reactive oxygen species (ROS) generated by different groups under microwave irradiation were detected using the DCFH-DA probe, confirming the significant microwave dynamic effect of Zr@C/C.(D-E) Survival rate of Heap1-6

cells incubated with different concentrations of zirconium dioxide@C/C nanoparticles and zirconium dioxide nanoparticles.(F-G) Survival rate of HUVEC cells incubated with different concentrations of zirconium dioxide@C/C nanoparticles and zirconium dioxide nanoparticles.

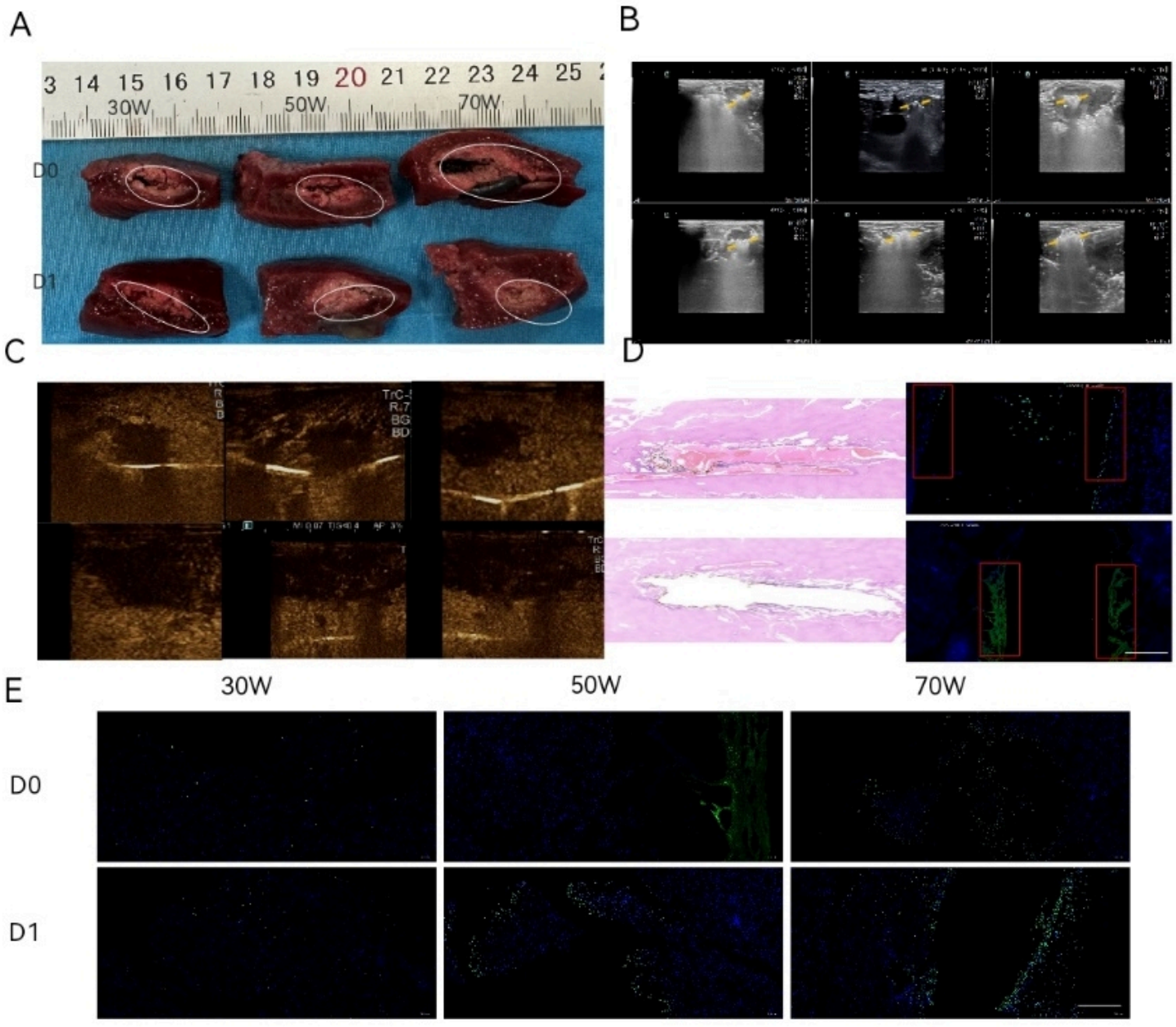


Figure 4

In vivo evaluation of Zr@C/CNPs + MWA on rabbit liver tumor models (ablation volume, residual tumor rate, recurrence rate).(A) Gross photographs of ex vivo liver ablation: Photographs of liver tissue sections from rabbit VX2 liver tumor models after ablation at different powers (30W, 50W, 70W), showing the size

and morphology of coagulative necrosis areas.(B) Intraoperative ultrasound monitoring images: Real-time ultrasound monitoring during ablation to track the position of the ablation needle and changes in hyperechoic masses generated during the ablation process.(C) Contrast-enhanced ultrasound (CEUS) evaluation: Comparison of contrast-enhanced ultrasound images before and after treatment (D0 vs D1), used to assess the complete ablation rate and local residual tumor through the range of non-perfused areas.(D) Comparison of liver ablation effects between the ex vivo rabbit liver drug group and the control group (HE, TUNEL staining): Histopathological observation of tissues at the edge and center of the ablation area, used to define the necrosis boundary and evaluate the protective effect on adjacent blood vessels.(E) TUNEL apoptosis staining: In situ terminal apoptosis marker staining of liver tissue sections, where green fluorescence represents apoptotic cells, used to evaluate the range of cell death induced by microwave dynamic therapy.

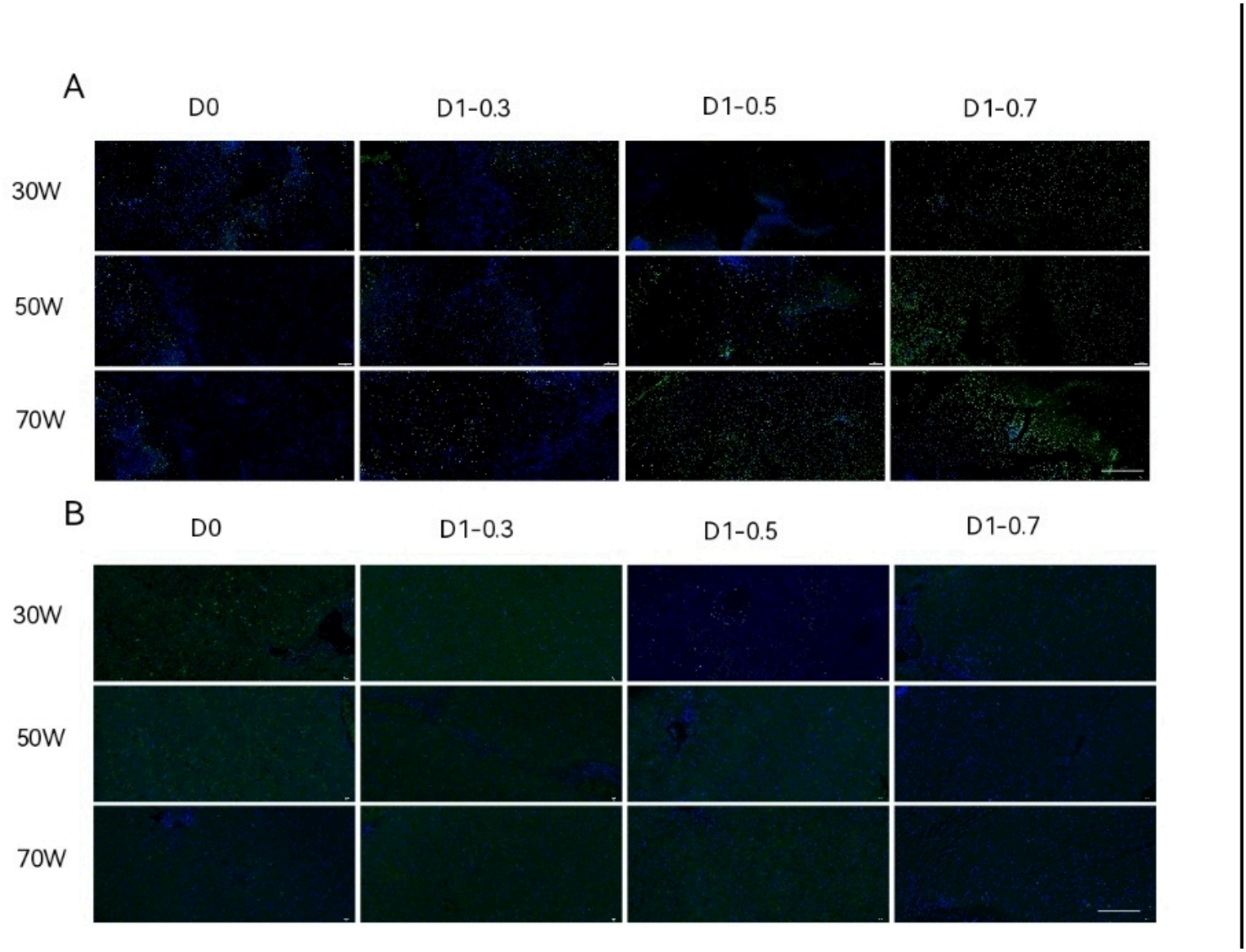


Figure 5

TUNEL apoptosis staining (A) and Ki67 staining (B) of ablated areas of ex vivo rabbit tumors under different drug concentrations and different ablation powers.

Supplementary Files

This is a list of supplementary files associated with this preprint. Click to download.

- Supplementarycontent.docx